

## Controlled Synthesis, Characterization, and Crystallization of Ni–P Nanospheres

Songhai Xie,<sup>†</sup> Minghua Qiao,<sup>†</sup> Wuzong Zhou,<sup>\*,‡</sup> Ge Luo,<sup>†</sup> Heyong He,<sup>†</sup> Kangnian Fan,<sup>\*,†</sup> Tiejun Zhao,<sup>§</sup> and Weikang Yuan<sup>§</sup>

Department of Chemistry and Shanghai Key Laboratory of Molecular Catalysis and Innovative Materials, Fudan University, Shanghai 200433, People's Republic of China, School of Chemistry, University of St. Andrews, St. Andrews, Fife KY16 9ST, United Kingdom, and UNILAB, State Key Laboratory of Chemical Reaction Engineering, East China University of Science and Technology, Shanghai 200237, People's Republic of China

Received: September 8, 2005; In Final Form: October 27, 2005

The size- and composition-controlled synthesis of Ni–P nanospheres from nickel chloride and sodium hypophosphite has been systematically investigated by changing the conditions, such as the ratio of the starting materials, pH value, and reduction temperature. It was found that when the starting ratio of  $\text{H}_2\text{PO}_2^-/\text{Ni}^{2+}$  was changed the size and chemical composition of the nanoparticles changed simultaneously. Within a suitable pH range, the phosphorus content was altered without affecting the particle size. Increasing the reduction temperature resulted in smaller Ni–P nanospheres but invariable phosphorus content. The Ni–P nanospheres were amorphous when the phosphorus content was higher than 10.0 mol %, while lower phosphorus content led to a composite of amorphous Ni–P and face-centered cubic (fcc) Ni. During postsynthesis calcinations, amorphous Ni–P nanospheres with a low phosphorus content directly crystallized to  $\text{Ni}_3\text{P}$  and fcc Ni. However, the specimens with high phosphorus content crystallized via some intermediate phases such as  $\text{Ni}_5\text{P}_2$  and  $\text{Ni}_{12}\text{P}_5$ . In the latter, an amorphous P-rich shell was developed simultaneously. A preliminary catalytic test of growth of carbon nanofibers on the Ni–P nanospheres has been carried out.

## I. Introduction

Phosphides form a large family of useful materials. Indium phosphide nanowires are promising in applications in polarization-sensitive nanoscale photodetectors, nanobarcodes, polarized nanoscale light-emitting diodes, and thin-film transistors.<sup>1,2</sup> Indium–gallium arsenide–phosphide has been used as photonic crystal to emit light at optical communication wavelengths.<sup>3</sup> While gallium phosphide can enhance the scattering efficiency of visible light,<sup>4</sup> manganese phosphide intercalates lithium ion reversibly with low potential, thus being promising for use in fabricating lithium batteries.<sup>5</sup> Many transition metal phosphides including Ni–P are superior catalysts in hydrodesulfurization and hydrodenitrogenation reactions.<sup>6–8</sup> In addition, Ni–P has been used in various composite coatings to modify the physical properties of the materials.<sup>9–11</sup>

It has been well-known that nanoparticles exhibit distinctive electronic and magnetic properties that differ from those in bulk.<sup>12–14</sup> However, only limited endeavors have been devoted to the synthesis of nanosized Ni–P particles,<sup>15–18</sup> and no systematic work has been conducted to gain an insight into the relationships between the preparation conditions and the dimension and homogeneity of the resulting Ni–P nanoparticles. In this work, we investigated in detail the effects of the molar ratio of  $\text{H}_2\text{PO}_2^-/\text{Ni}^{2+}$ , pH value, and reaction temperature on the size and composition of the nanospherical Ni–P alloys. We demonstrate that control of the size and composition of the Ni–P nanoparticles is feasible.

## II. Experimental Section

Ni–P nanospheres were synthesized by a reaction of nickel chloride and sodium hypophosphite. In a typical synthesis, 21.0 mmol of nickel chloride, 47.2 mmol of sodium hypophosphite, and 36.7 mmol of sodium acetate were dissolved in 100 mL of water in a three-necked flask and maintained at 363 K. The pH value was adjusted by a potassium hydroxide solution. Weighted KOH was dissolved in 70 mL of water and then transferred into the above solution. High-purity nitrogen (99.9999%) was used as the sheltering gas. After an incubation period of ca. 50 min, the black precipitate appeared and hydrogen gas evolved simultaneously. The precipitate was separated by centrifugation (3000 rpm for 10 min) and washed with 8 M ammonia ( $\sim 30$  mL) twice, distilled water ( $\sim 30$  mL) thrice, and absolute ethanol ( $\sim 30$  mL) thrice sequentially. The resulting Ni–P samples were soaked in absolute ethanol before characterization. Three series of Ni–P samples were prepared by adjusting the molar ratio of  $\text{H}_2\text{PO}_2^-/\text{Ni}^{2+}$ , pH, and reaction temperature in the above procedure and designated as R-*x*, P-*y*, and T-*z*, respectively, with *x*, *y*, and *z* denoting the values of the nominal ratio of  $\text{H}_2\text{PO}_2^-/\text{Ni}^{2+}$ , pH, and temperature in kelvin. All of the reagents were analytical reagent grade, and the water used was double-distilled.

The bulk compositions of the samples were analyzed by inductively coupled plasma atomic emission spectroscopy (ICP-AES, IRIS Intrepid).

Scanning electron microscopy (SEM) images were recorded on a Philips XL 30 electron microscope. The accelerating voltage was in a range of 20–30 kV. The sample was attached with conductive double-sided carbon adhesive tape on an aluminum slab without gold coating.

\* Authors to whom correspondence should be addressed. E-mail: wzhou@st-andrews.ac.uk; knfan@fudan.edu.cn.

<sup>†</sup> Fudan University.

<sup>‡</sup> University of St. Andrews.

<sup>§</sup> East China University of Science and Technology.

Transmission electron microscopy (TEM) observation was carried out on a JEOL JEM-2011 electron microscope operated at 200 kV, with a point resolution of 0.23 nm. The powder specimen was dispersed in absolute ethanol and sonicated for  $\sim 1$  min. One drop of the suspension was deposited on a specimen grid coated with a holey carbon film. The images were recorded using a Gatan 794 charge coupled device (CCD) camera ( $1000 \times 1000$  pixels). The average size and size distribution of each specimen were evaluated from about 300 randomly selected particles.

Energy-dispersive X-ray microanalysis (EDX) was performed using an Oxford INCA energy analyzer with a Si(Li) detector attached to the microscope. The chemical compositions of the specimens were evaluated by a quantitative analysis program with the XPP (matrix correction scheme developed by Pouchou and Pichior) correction procedure.<sup>19</sup> The beam spot was chosen in a range of 15–25 nm.

Powder X-ray diffraction (XRD) patterns were recorded on a Bruker Advanced D8 powder X-ray diffractometer using Ni-filtered Cu K $\alpha$  radiation. The tube voltage and current were 40 kV and 40 mA, respectively. To monitor the crystallization behavior of the Ni–P samples, a hot specimen stage was used. The Ni–P sample with the storage liquid was placed on a hot specimen plate and heated with a step of 50 K and retained for 10 min at each stage for the XRD scanning. Throughout the data collection, the hot stage was purged with argon flow (99.9995%) to avoid oxidation.

The chemical states of the Ni–P samples were detected by X-ray photoelectron spectroscopy (XPS) on a Perkin-Elmer PHI 5000C system. The spectra were recorded with the Mg K $\alpha$  line ( $h\nu = 1253.6$  eV) as the excitation source. The sample was pressed into a disk (10 mm in diameter and 1 mm in thickness) and kept in ethanol before mounting on the sample plate. It was degassed in the pretreatment chamber at 383 K for 2 h in vacuo before being transferred into the analyzing chamber where the background vacuum was better than  $2 \times 10^{-9}$  Torr.

### III. Results and Discussion

**1. Synthesis of Ni–P Nanospheres. A. Effect of the  $\text{H}_2\text{PO}_2^-/\text{Ni}^{2+}$  Molar Ratio.** We consider first the effect of the molar ratio of  $\text{H}_2\text{PO}_2^-/\text{Ni}^{2+}$  on the size of the amorphous Ni–P nanoparticles. The nominal molar ratio of  $\text{H}_2\text{PO}_2^-/\text{Ni}^{2+}$  was changed from 2.2 to 11.0, and the corresponding products were designated as R-2.2, R-4.4, R-6.6, R-8.8, and R-11.0, respectively. Other conditions were fixed at a pH of 12.6 and reaction temperature of 363 K. Figure 1 shows TEM images of the as-prepared samples. It is observed that, with the increment of the  $\text{H}_2\text{PO}_2^-/\text{Ni}^{2+}$  ratio, the average particle size decreases monotonically from 82.1 to 26.9 nm. Moreover, the particles in each sample seem to be quite uniform in size, exhibiting a narrow size distribution with a standard deviation within 4.0%. One typical histogram is shown in Figure 1f, and the whole set of size distribution histograms is shown in the Supporting Information (Figure S1). It is worth noting that, to our knowledge, the R-11.0 sample has the smallest particle size that has ever been reported for Ni–P. The effect of the  $\text{H}_2\text{PO}_2^-/\text{Ni}^{2+}$  ratio on the particle size can be explained using a surface electrical double-layer model. It is anticipated that the surface of the produced Ni–P nanoparticles tends to be covered by anions such as  $\text{H}_2\text{PO}_2^-$  because of the electron donation characteristics.<sup>18</sup> At a higher  $\text{H}_2\text{PO}_2^-/\text{Ni}^{2+}$  ratio, more  $\text{H}_2\text{PO}_2^-$  ions are adsorbed on the surface of the Ni–P particles, forming an electrical double-layer. The resulted Coulombic repulsion will reduce the rate of further particle aggregation.<sup>20</sup>

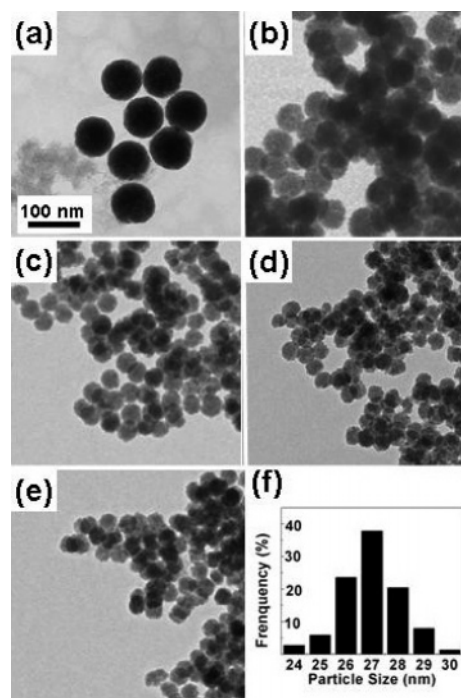


**Figure 1.** TEM images of R-series Ni–P amorphous nanospheres, prepared using different starting ratios of  $\text{H}_2\text{PO}_2^-/\text{Ni}^{2+}$ , with particle sizes of (a)  $82.1 \pm 1.1$  nm, (b)  $57.0 \pm 1.4$  nm, (c)  $38.0 \pm 1.2$  nm, (d)  $30.1 \pm 1.1$  nm, and (e)  $26.9 \pm 1.2$  nm. The images were recorded at the same magnification. The corresponding  $\text{H}_2\text{PO}_2^-/\text{Ni}^{2+}$  ratios are (a) 2.2, (b) 4.4, (c) 6.6, (d) 8.8, and (e) 11.0, respectively. (f) Particle size distribution of specimen R-11.0.

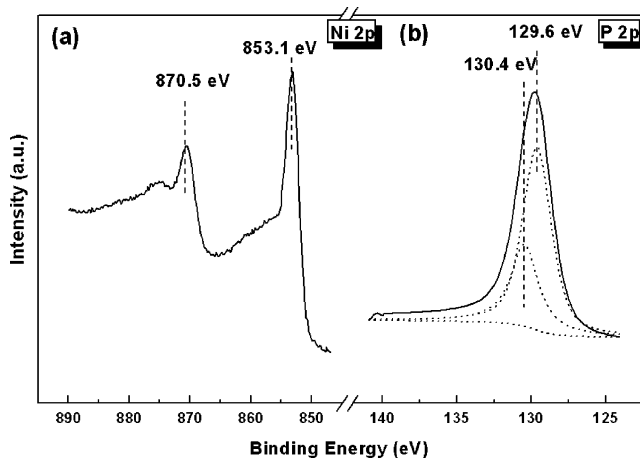


**Figure 2.** Typical XPS spectra of the R-series nanospheres (a) Ni 2p and (b) P 2p.

XPS characterization revealed that Ni and P in the as-prepared Ni–P nanospheres were solely in their elemental states and no other elements were detected. Figure 2a shows typical XPS spectra from the R-series specimens. There are only two peaks at 853.1 and 870.5 eV, attributable to the Ni 2p<sub>3/2</sub> and Ni 2p<sub>1/2</sub> energy levels, respectively. In the P 2p spectrum (Figure 2b), deconvolution results in two peaks at 129.6 and 130.4 eV with an intensity ratio of 2:1, which can be readily assigned to the doublet of elemental phosphorus.<sup>21</sup>

It has been found previously that the initial  $\text{H}_2\text{PO}_2^-/\text{Ni}^{2+}$  ratio can influence the chemical composition of the Ni–P alloys.<sup>22</sup> In the present work, the EDX results indicated that when the  $\text{H}_2\text{PO}_2^-/\text{Ni}^{2+}$  ratio was increased from 2.2 to 11.0 the phosphorus content in the produced nanospheres increased moderately from 19.0 to 24.8 mol % (Figure 3a). Generally, the

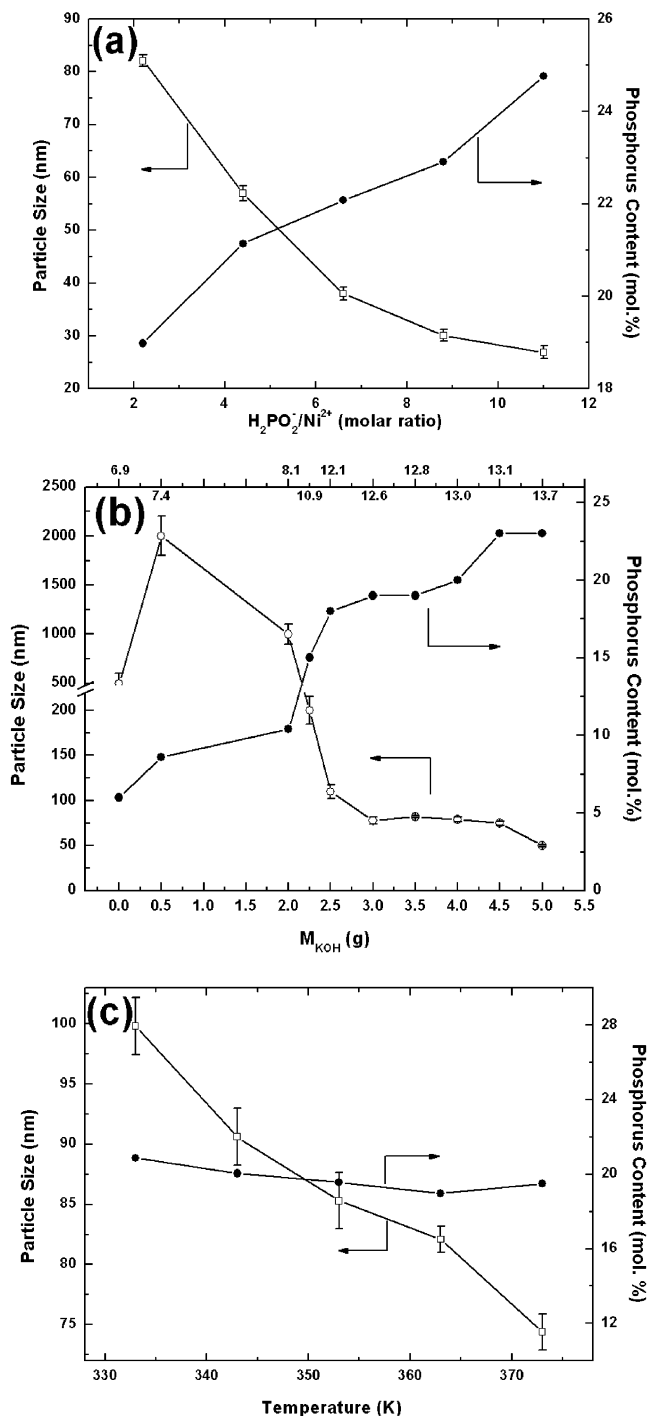


**Figure 3.** Particle size and phosphorus content of the Ni–P nanospheres plotted as a function of (a) the initial  $\text{H}_2\text{PO}_2^-/\text{Ni}^{2+}$  molar ratio, (b) the mass of KOH ( $M_{\text{KOH}}$ ) added, and (c) the reaction temperature. The pH value corresponding to each  $M_{\text{KOH}}$  value is shown on the top axis of part b.

reduction of nickel is first-order with respect to the concentration of hypophosphite

$$\frac{d\text{Ni}^0}{dt} \propto [\text{H}_2\text{PO}_2^-]$$

and a second-order dependence on hypophosphite was found for phosphorus deposition<sup>23,24</sup>

$$\frac{d\text{P}}{dt} \propto [\text{H}_2\text{PO}_2^-]^{1.91}$$

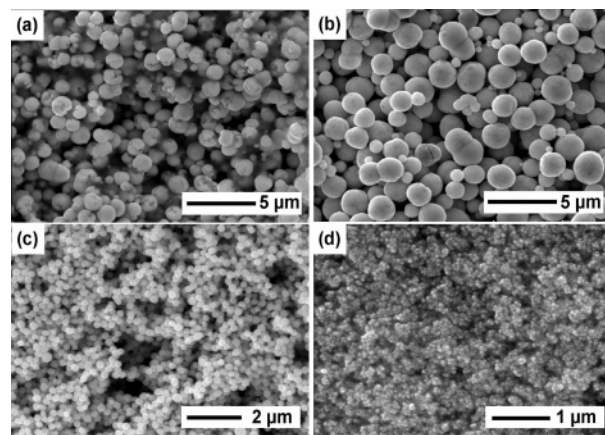


**Figure 4.** SEM images of the specimens (a) P-6.9, (b) P-7.4, (c) P-10.9, and (d) P-12.8 recorded at different magnifications.

Thus, it can be understood that increasing the  $\text{H}_2\text{PO}_2^-$  concentration will kinetically increase the phosphorus content in the Ni–P particles.

**B. Effect of pH.** When preparing the P-series samples, the acidity of the solution was adjusted by KOH, while other reaction conditions were kept the same as described in the Experimental Section. The pH value was varied from 6.9 to 13.7, corresponding to the amount of added KOH from 0 to 5.0 g. In Figure 3b, it is found that when the pH of the solution is lower than 7.4 the sizes of the Ni–P particle are in the micrometer range and increase sharply with the pH value. For example, the mean particle sizes of P-6.9 and P-7.4 are ca. 0.5 and 2 μm, respectively. The size distributions of these samples are relatively wide, as indicated by the SEM images (Figures 4a and 4b). Thereafter, the size of the Ni–P particles reduces drastically (Figure 3b) and meanwhile becomes much more uniform (Figures 4c and 4d). The effect of pH value on the size of the Ni–P particles is expected to be analogous to that of  $\text{H}_2\text{PO}_2^-$ . Although this effect is not obvious in the low pH range, in the pH range from 7.4 to 12.6,  $\text{OH}^-$  anions will contribute to the electrical double-layer on the surface of the nanoparticles and, therefore, suppress the particle growth. In the higher pH range, however, the size of the Ni–P particles does not decrease further. For example, when the amount of KOH is increased from 3.0 to 4.5 g, the particle size remains almost constant at ca. 75 nm. Such a phenomenon is related to the buffering effect of NaOAc, which stabilizes the pH of the solution at 12.6–13.1. This is another evidence of the pH dependence of the particle size. However, Figure 3b shows that the phosphorus content in the Ni–P nanospheres increases monotonically within the pH range investigated. This is probably due to the formation of  $\text{Ni}(\text{OH})_2$  or  $\text{Ni}(\text{OH})_x$ , reducing the relative concentration of  $\text{Ni}^{2+}$  in the reaction system. Within the pH range of 12.6–13.1, one can easily obtain Ni–P nanospheres with similar sizes but different compositions, which is desirable for the investigation of the compositional effect on the physicochemical properties of the Ni–P particles without possible interference of the size effect. When the pH was 13.7, even smaller Ni–P particles were produced, as shown in Figure 3b. However, there are oxidized nickel species that cannot be washed away from the Ni–P nanospheres by ammonia as confirmed by EDX. This result can be interpreted as that stronger basic condition favors the formation of  $\text{Ni}(\text{OH})_2$ , which is less reducible than  $\text{Ni}^{2+}$  by sodium hypophosphite.<sup>25</sup>

It would be instructive to compare our results with the previous ones, although there are only limited nonsystematic studies specifying the pH during the preparation of Ni–P



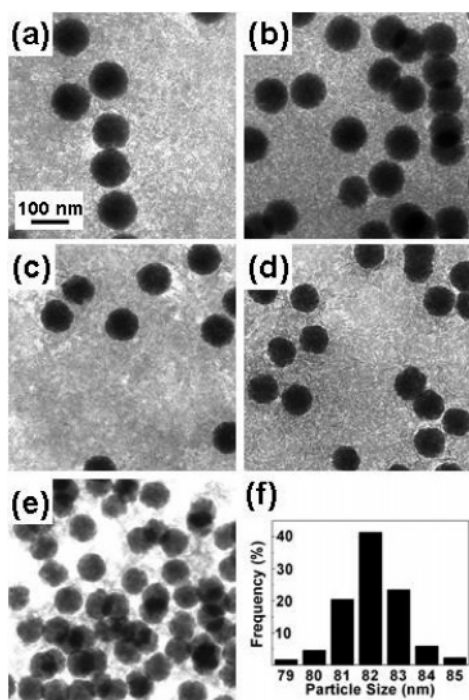


**Figure 5.** TEM image of the T-series Ni–P specimens recorded at the same magnification, showing particle sizes and morphologies of the Ni–P nanospheres prepared at different reaction temperatures: (a) 333, (b) 343, (c) 353, (d) 363, and (e) 373 K. (f) Particle size distribution of specimen T-363.

particles. At pH 11, Deng et al. obtained Ni–P particles with an average size of about 70 nm.<sup>15</sup> Under similar reaction conditions but initiated by a drop of  $\text{KBH}_4$ , Ni–P particles with diameters of about 100 nm were synthesized.<sup>26</sup> At pH 11, Chen and co-workers prepared Ni–P particles with a minimum size of about 250 nm.<sup>18,25</sup> These results correspond well with the trend plotted in Figure 3b.

**C. Effect of Reaction Temperature.** To accelerate the reduction process, a reaction temperature of 363–368 K is usually employed for the preparation of Ni–P alloys, while the effect

of temperature on the particle size has never been explored. In the present work, on the basis of the preparation conditions for R-2.2 with pH 12.8, we produced the T-series samples by varying the reduction temperature. The corresponding TEM images are shown in Figure 5. It was found that when the temperature was changed from 333 to 373 K the particle size of Ni–P decreased continuously from 99.8 to 74.4 nm (Figure 3c); meanwhile the incubation period was reduced from 17 to 0.5 h. It has been established that as the reduction temperature is increased the reaction rate increases exponentially.<sup>24</sup> A faster reaction rate usually results in smaller Ni–P particles, as confirmed by our TEM observation. Analysis of the particle size distribution reveals that the standard deviations are always less than 5%. In particular, the T-363 sample has the narrowest particle size distribution with a standard deviation of  $\sim 1\%$  (Figure 5f). The histograms of size distributions of other specimens are given in the Supporting Information (Figure S2).

It is reported that the composition of the Ni–P films prepared by electroless plating can only be slightly altered by merely changing the temperature of solutions.<sup>24</sup> The result obtained in the present work agrees with this conclusion. Figure 3c shows that the phosphorus content in the Ni–P nanospheres remains at ca. 19.5 mol % irrespective of the reduction temperature. Thus the reduction temperature can be a useful parameter for controlling the size of the Ni–P nanospheres only.

**2. Structure of the Ni–P Nanospheres.** A typical XRD pattern for the R- and T-series Ni–P samples is shown in Figure 6a. The only broad peak centered at  $2\theta$  of about  $44.6^\circ$  suggests the noncrystalline structure of the as-prepared Ni–P particles, which is confirmed by the selected area electron diffraction (SAED) pattern (Figure 6b) showing a halo ring rather than distinct dots.<sup>27,28</sup> Narrow beam diffraction (NBD) with the electron beam smaller than  $10 \text{ nm}^2$  was employed to further prove the amorphous character of individual nanospheres (inset of Figure 6b).

More detailed structures were revealed by high-resolution transmission electron microscopy (HRTEM). Figure 6c shows a typical HRTEM image from specimen R-11.0. The structure is basically disordered. However, there are some partially

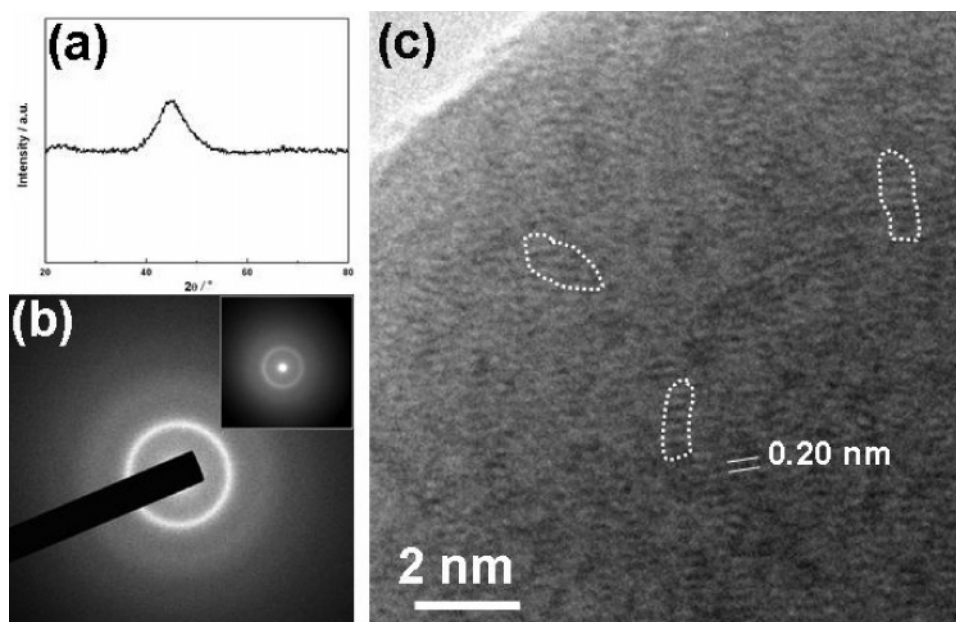


**Figure 6.** (a) Typical XRD pattern of the R- and T-series Ni–P alloys. (b) SAED pattern of several Ni–P nanospheres and NBD pattern (inset) from a single Ni–P nanosphere. (c) HRTEM image recorded on a single Ni–P nanosphere. The areas marked with dotted lines are some examples of short-range ordered nanodomains.

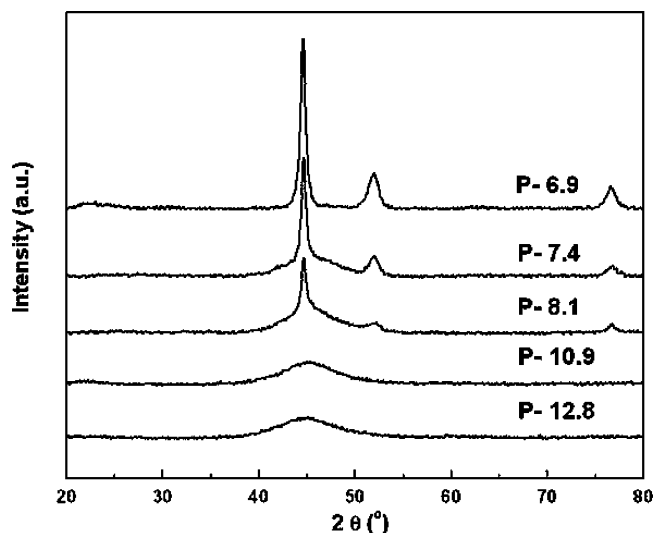


**Figure 7.** XRD patterns of the P-series of Ni–P alloys. The patterns of the specimens P-12.1, P-12.6, P-13.0, P-13.1, and P-13.7 are almost the same as P-12.8 and not shown in the figure.

ordered nanodomains as verified by the short-range lattice fringes, with the dimension as small as 1 nm. The  $d$ -spacing of these fringes in the domains is  $\sim 0.20$  nm, which correlates well with the broad XRD peak with  $2\theta$  of  $\sim 44.6^\circ$ . Since the dimension of the nanodomains is beyond the detection limits of SAED and EDX, the structure and composition of the nanodomains cannot be determined. However, since these nanodomains are dominant in the amorphous Ni–P sample, we believe that they have similar composition as the bulk.

For the P-series samples, XRD reveals that the structure is not always amorphous, but rather it depends strongly on the pH value (Figure 7). For sample P-6.9 without the addition of KOH, three sharp peaks with  $2\theta$  at  $44.6^\circ$ ,  $52.0^\circ$ , and  $76.8^\circ$  are observed, which can be indexed to the (111), (200), and (220) reflections, respectively, from the face-centered cubic (fcc) Ni phase.<sup>29</sup> With the increment of the pH value, the diffraction peaks due to fcc Ni are attenuated, while the broadness of the peak at  $44.6^\circ$  is increased. At pH 10.9 or above, the peaks due to fcc Ni are no longer discernible, and the XRD patterns are similar to that in Figure 6a. It has been noted from the literature that the Ni–P alloys with low phosphorus content are either crystalline<sup>30</sup> or consist of microcrystalline nickel grains.<sup>31</sup> As inferred by the relation between the composition and the pH value (Figure 3b) and the pH-dependent structures (Figure 7), the turning point from the amorphous Ni–P/crystalline Ni composite to the totally amorphous Ni–P is near the phosphorus content of approximately 10.0 mol %.

**3. Thermal Behavior of the Ni–P Nanospheres.** High-temperature XRD characterizations were carried out using specimens R-2.2 and R-11.0 as examples to illustrate the effect of phosphorus content on the crystallization behavior of the amorphous Ni–P nanospheres (Figure 8). From room temperature to 373 K, both samples gave only a broad peak at  $44.6^\circ$ . In the range of 373–523 K, the intensity of the broad peak increases gradually, possibly due to the growth of the short-range ordered nanodomains. When the temperature was further increased to 573 K, different crystallization behaviors were observed. For specimen R-2.2 with a phosphorus content of 18.6 mol %, there are four diffraction peaks at  $41.6^\circ$ ,  $44.3^\circ$ ,  $51.7^\circ$ , and  $76.1^\circ$ . The peak at  $41.6^\circ$  can be indexed to the (231) reflection from the  $\text{Ni}_3\text{P}$  phase, while the others are attributed to the fcc nickel phase.<sup>29</sup> These peaks grew up continuously at higher temperatures. Above 723 K, the diffraction peaks at

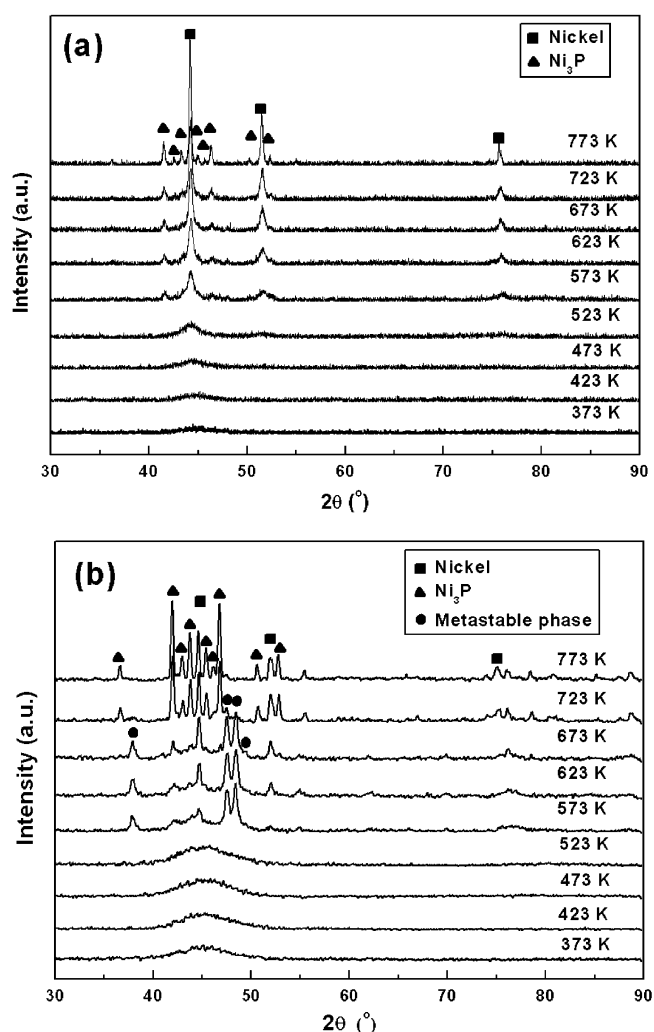


**Figure 8.** In situ high-temperature XRD patterns of (a) R-2.2 and (b) R-11.0 with compositions of  $\text{Ni}_{81.4}\text{P}_{18.6}$  and  $\text{Ni}_{76.2}\text{P}_{23.8}$ , respectively.

$42.7^\circ$ ,  $43.3^\circ$ ,  $45.0^\circ$ ,  $45.7^\circ$ ,  $46.3^\circ$ ,  $50.3^\circ$ , and  $52.3^\circ$  are discerned, corresponding to the (330), (112), (240), (202), (141), (222), and (132) reflections of the  $\text{Ni}_3\text{P}$  phase, respectively. The calculated dimensions of the tetragonal unit cell are  $a = 0.8952$  nm and  $c = 0.4388$  nm. It is noted that at 773 K there is no hump around  $2\theta$  of  $44.6^\circ$ , indicating a complete crystallization of the amorphous Ni–P nanoparticles with fcc Ni as the dominant phase (Figure 8a).

However, the R-11.0 sample with a higher phosphorus content exhibits a much more complex crystallization behavior (Figure 8b). At 573 K, six diffraction peaks emerge at  $37.9^\circ$ ,  $42.7^\circ$ ,  $44.7^\circ$ ,  $47.6^\circ$ ,  $48.5^\circ$ , and  $76.3^\circ$ , resulting from three different phases specified as follows. The peaks at  $37.9^\circ$ ,  $47.6^\circ$ , and  $48.5^\circ$  are attributable to the metastable phases of  $\text{Ni}_{12}\text{P}_5$  and  $\text{Ni}_5\text{P}_2$ ,<sup>32–37</sup> while the peaks at  $44.7^\circ$  and  $76.3^\circ$  are due to the {111} and {220} planes of fcc Ni. The peak at  $42.7^\circ$  is assigned to the {330} planes of the  $\text{Ni}_3\text{P}$  phase. The metastable phases remained stable until 723 K, at which the peaks due to the metastable phases diminished and the peaks due to  $\text{Ni}_3\text{P}$  were well developed. Meanwhile, the peaks of fcc Ni were intensified. The XRD pattern for the completely crystallized R-11.0 sample only shows the sharp peaks for fcc Ni and  $\text{Ni}_3\text{P}$ . Contrary to that of R-2.2, the diffraction peaks due to  $\text{Ni}_3\text{P}$  are much stronger than those of fcc Ni, which can be attributed to the higher phosphorus content in the R-11.0 sample.

Our high-temperature XRD results of the amorphous Ni–P nanospheres are consistent with previous observations on Ni–P

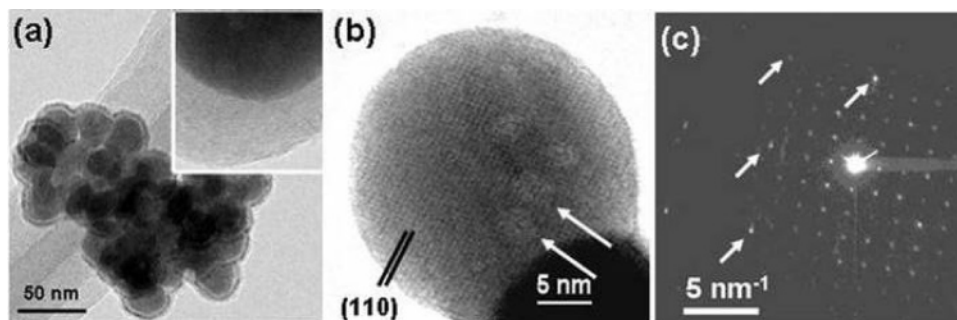


**Figure 9.** (a) TEM image of the specimen R-11.0 after heat treatment at 723 K. The inset is an enlarged TEM image of a part of a nanosphere. (b) HRTEM image of a whole nanosphere showing crystalline  $\text{Ni}_3\text{P}$  structure. The arrows indicate some Ni nanodomains. (c) SAED pattern from a small area of a nanosphere showing overlapping of two patterns viewed down the  $[001]$  zone axes of  $\text{Ni}_3\text{P}$  and fcc Ni (indicated by the arrows), respectively.

films prepared by electroless plating. Hur and co-workers revealed that Ni–P films containing less than 7 wt % of phosphorus transform directly into  $\text{Ni}_3\text{P}$  and crystalline Ni, with the former embedded in the matrix of the latter. For Ni–P deposits with 10.1–13.6 wt % P, phase transformation passes through several off-stoichiometric metastable phases such as  $\text{Ni}_5(\text{P,Ni})_2$ , and  $\text{Ni}_3(\text{P,Ni})$ .<sup>38</sup> In another case, Ma et al. identified the metastable  $\text{Ni}_{12}\text{P}_5$  phase before transformation to crystalline nickel and  $\text{Ni}_3\text{P}$  for a high-P deposition (12.1 wt % P).<sup>39</sup> Similar phase transformation from amorphous Ni–P to crystalline Ni and  $\text{Ni}_3\text{P}$  directly and via intermediate phases were also discussed in some recently published reports.<sup>40–42</sup>

Considering the Ni/P atomic ratio of  $\sim 3:1$  for the R-11.0 sample, it is very interesting to see that crystallization resulted in substantial amount of fcc Ni, while no P or other P-rich phases were detected by XRD. For the Ni–P sample with an even lower Ni/P ratio, Keong et al. also observed similar crystallization products.<sup>37</sup> Using a three-dimensional atomic probe, Cerezo et al. found that in Ni–P alloys phosphorus would segregate from the alloys and may form an amorphous phase dispersed on the substrate.<sup>43</sup> If there was pure phosphorus phase in our products, considering the boiling point (553.3 K) of white phosphorus and the sublime point (689 K) of red phosphorus,<sup>44</sup> both are much lower than the temperature used in the present heat treatment (773 K), then the chance was high for phosphorus to escape from the bulk of the Ni–P alloy, resulting in a decrease of the phosphorus content. However, the above assumption is in conflict with our ICP-AES results, which identified that, before and after heat treatment, the phosphorus contents were  $18.6 \pm 0.5$  and  $19.0 \pm 0.5$  mol % for the sample of R-2.2 and  $23.8 \pm 0.5$  and  $23.0 \pm 0.5$  mol % for R-11.0. Considering the experimental error, we can see that the compositions of the specimens did not change; i.e., the loss of phosphorus was not observed. Consequently, we believe that the formation of an amorphous P-rich phase rather than segregated pure phosphorus is more likely in the present case.

Figure 9a is a TEM image of the R-11.0 sample after heat treatment at 723 K under an Ar atmosphere. It is shown that the nanospheres developed a unique core–shell structure and merged into larger clusters. As examined by EDX, the molar ratio of Ni:P in the core area is close to 3.0, while it is about 1.3 in the shell, indicative of the enrichment of phosphorus in the shell. The inset of Figure 9a shows an enlarged image, revealing the amorphous nature of the shell.

However, the cores of the nanospheres after the heat treatment are crystalline. Figure 9b is an HRTEM image of a whole crystalline nanosphere. The  $d$ -spacing of the fringes is about 0.6 nm, corresponding to (110) planes in the  $\text{Ni}_3\text{P}$  structure. The nanosphere looks like a single crystal. However, there are

some nanodomains embedded in the  $\text{Ni}_3\text{P}$  crystalline network, as indicated by the arrows. Although no atomic lattice fringes of these domains could be revealed due to the limited resolution of the microscope and strong background of the  $\text{Ni}_3\text{P}$  image, we used the SAED technique to find that these domains were most likely to be fcc Ni nanocrystallites. The SAED pattern in Figure 9c was recorded from a small area of a nanosphere, showing an overlap of two diffraction patterns. The square pattern with larger  $d$ -spacings (ca. 0.6 nm) is from the (110) plane of tetragonal  $\text{Ni}_3\text{P}$ , and the second, indicated by the arrows, has a principal  $d$ -spacing of 0.174 nm, corresponding to the (200) planes of fcc Ni with the unit cell parameter  $a = 0.35$  nm. The observation confirms the XRD results and further reveals the detailed structure of the nanospheres after heat treatment: crystalline  $\text{Ni}_3\text{P}$  with randomly embedded fcc Ni nanodomains.

**4. Growth of Carbon Nanofibers Using the Ni–P Nanospheres as Catalysts.** Ni– $\text{Ni}_3\text{P}$  alloy films have been used as catalysts for the formation of carbon nanofibers (CNFs) using the thermal chemical vapor deposition (CVD) method, whereas Ni– $\text{Ni}_3\text{P}$  nanocrystalline catalysts yielded the formation of carbon nanotubes (CNTs). It was proposed that the Ni element in the alloy catalysts may serve as a catalyst for the growth of carbon nanofibers and nanotubes.<sup>45,46</sup> In the present work, the as-synthesized R-2.2 and R-11.0 nanospheres were used as catalysts for the growth of carbon nanofibers.

The Ni–P nanospheres were deposited in a quartz boat that was placed in the middle of a tube furnace. The rate of input flow of a mixed gas, 25% (v/v)  $\text{H}_2/\text{Ar}$ , was controlled at  $1.0 \text{ mL min}^{-1}$ . The catalyst was heated at 873 K for about 3 h. The input gas was then switched to  $\text{C}_2\text{H}_6/\text{H}_2$  (1:2, v/v) with a flow rate of  $150 \text{ mL min}^{-1}$  at standard temperature and pressure. The reaction was carried out at 923 K for 4 h.

The produced carbon nanofibers were examined by HRTEM. Figure 10a shows the CNFs with an almost uniform diameter of about 50 nm produced on R-11.0, which has an average diameter of 26.9 nm (Figure 3a). The diameter of CNFs produced on R-2.2 (82.1 nm in diameter, Figure 3a) increased to about 150 nm (Figure 10b). The detailed structure of the CNFs contains graphitic layers stacking up along the nanofiber axis as shown in Figure 10c. There are several points that draw our attention. First, since the size distribution of the Ni–P nanospheres is very narrow and the diameters of the CNFs are closely related to the size of the Ni–P particles, in principle, we can therefore produce CNFs with expected diameters (about doubled from the diameters of the catalytic particles) that cannot be achieved on the Ni–P films.<sup>45,46</sup> This is an obvious advantage of applying our Ni–P nanospheres. Second, we do not observe any carbon nanotubes. Third, at the reaction temperature, the



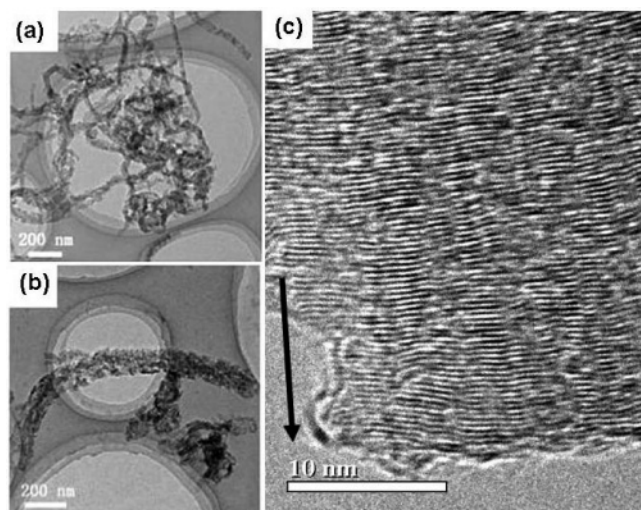


**Figure 10.** Low-magnification images of CNFs prepared (a) with R-2.2 and (b) with R-11.0. (c) HRTEM image of CNFs grown on R-11.0, showing graphitic layers stacking up along the nanofiber axis indicated by the arrow.

Ni–P nanospheres must undergo crystallization (Figure 8). The HRTEM image of Figure 9 reveals that the Ni nanodomains are embedded in the  $\text{Ni}_3\text{P}$  crystalline network. If this structure is typical for the real catalytic particles, then the  $\text{Ni}_3\text{P}$  phase must play an important role in the catalytic reaction. Finally, the detailed structure shown in Figure 10c is different from that of CNFs grown on Ni–P films and is of great interest because the density of the open edges of graphitic layers (often act as active centers) on the surface of the nanofibers is very high.

The formation mechanism of the CNFs is yet to be fully understood. It has been previously observed that the formation of different carbon nanostructures is greatly affected by the shape of the catalytic particles. General speaking, three steps are involved in the CVD process of formation of carbon nanostructures. First, carbon-containing gas molecules are decomposed on the surface of catalytic metal particles into active carbon species. Second, the carbon species diffuse into the catalytic particles until a supersaturation of carbon is reached. Third, the segregation and crystallization of carbon takes place on the surface of the metal particles. During the above three steps, the reconstruction of the metal particle is often observed.<sup>47</sup> The fluidity of carbon-containing metal particles plays a fundamental role in the formation of carbon nanostructures.<sup>48</sup> CNFs often form on some plateletlike catalytic particles, while CNTs are more likely to form on spherical particles. There is not a clear border of experimental conditions for these two phases, and some intermediate structures, such as carbon nanobells, may also be produced.<sup>49</sup> Figure S3 in the Supporting Information shows a Ni–P particle after the catalytic reaction for growing CNFs. The morphology of the particle has changed from spherical to plateletlike, and the latter was maintained when the temperature was cooled to room temperature. Consequently, the first possible reason for the formation of CNFs in the present work is that the catalytic nanospheres became plateletlike at high temperature during the catalytic reaction. The diameters of the nanospheres increased accordingly, and it can be explained that the diameters of produced CNFs are significantly larger than that of the original Ni–P nanospheres. The second possible reason is related to the imperfect carbon sheets in the CNFs as seen in Figure 10c. The produced CNFs contain a large number of defects, making more difficulties in the formation of CNTs.

#### IV. Conclusions

On the basis of this systematic investigation, we found that the nominal  $\text{H}_2\text{PO}_4^-/\text{Ni}^{2+}$  ratio, pH, and reduction temperature can affect the size and composition of the Ni–P nanospheres in different ways. At least under the experimental conditions used in the present work, we can change the size of amorphous Ni–P nanospheres from 27 nm to 2  $\mu\text{m}$  and tune the phosphorus content in a range from 3 to  $\sim 25$  mol %. It is particularly important that, within a suitable pH range (e.g., 12.6 to 13.1), we can tune the phosphorus content when the particle size is unchanged. The behavior of crystallization of the Ni–P nanospheres is affected by the phosphorus concentration. They either form  $\text{Ni}_3\text{P}$  and fcc Ni directly with low levels of the phosphorus content or form some metastable  $\text{Ni}_{12}\text{P}_5$  and  $\text{Ni}_5\text{P}_2$  phases with high phosphorus concentrations during the crystal growth into  $\text{Ni}_3\text{P}$  and Ni. The crystalline nanospheres are coated by a P-rich shell, and the core structure is basically  $\text{Ni}_3\text{P}$  with randomly embedded fcc Ni nanodomains. Our preliminary catalytic studies indicate that the Ni–P nanospheres can be used as catalysts for synthesis of carbon nanofibers with narrow distributions of the diameters. More importantly, the structure of the carbon nanofibers contains graphitic layers stacking up along the nanofiber axis. The knowledge gained in the present work is believed to be useful in development of Ni–P and other phosphorus-containing industrial materials. Further investigations of local structures by  $^{31}\text{P}$  NMR and catalytic properties of the Ni–P nanospheres are being carried out in these laboratories.

**Acknowledgment.** This project was supported by the State Key Basic Research Development Program (G2000048009), the NSFC (20203004, 20273015, 20506004) and the Shanghai Science and Technology Committee (02ZA14006, 03QB14004).

**Supporting Information Available:** Particle size distributions of the R-series and T-series Ni–P nanospheres and a TEM image of a Ni–P particle after reaction for growing carbon nanofibers. This material is available free of charge via the Internet at <http://pubs.acs.org>.

#### References and Notes

- (1) Gudixsen, M. S.; Lauhon, L. J.; Wang, J.; Smith, D. C.; Lieber, C. M. *Nature* **2002**, *415*, 617.
- (2) Duan, X.; Huang, Y.; Wang, J.; Cui, Y.; Lieber, C. M. *Nature* **2001**, *409*, 66.
- (3) Ogawa, S. P.; Imada, M.; Yoshimoto, S.; Okano, M.; Noda, S. *Science* **2004**, *305*, 227.
- (4) Schuurmans, F. J. P.; Vanmaekelbergh, D.; van de Lagemaat, J.; Legendijk, A. *Science* **1999**, *284*, 141.
- (5) Souza, D. C. S.; Pralong, V.; Jacobson, A. J.; Nazar, L. F. *Science* **2002**, *296*, 1012.
- (6) Oyama, S. T.; Wang, X.; Lee, Y. K.; Chun, W. J. *J. Catal.* **2004**, *221*, 263.
- (7) Oyama, S. T. *J. Catal.* **2003**, *216*, 343.
- (8) Oyama, S. T.; Clark, P.; Wang, X.; Shido, T.; Iwasawa, Y.; Hayashi, S.; Ramallo-López, J. M.; Requejo, F. G. *J. Phys. Chem. B* **2002**, *106*, 1913.
- (9) Park, S. J.; Jang, Y. S. *J. Colloid Interface Sci.* **2003**, *263*, 170.
- (10) Reddy, V. V. N.; Ramamoorthy, B.; Nair, P. K. *Wear* **2000**, *239*, 111.
- (11) Leon, C. A.; R Drew, A. L. *J. Mater. Sci.* **2000**, *35*, 4763.
- (12) Volokitin, Y.; Sinzig, J.; de Jongh, L. J.; Schmid, G.; Vargaftik, M. N.; Moiseev, I. I. *Nature* **1996**, *384*, 621.
- (13) Cox, A. J.; Louderback, J. G.; Apsel, S. E.; Bloomfield, L. A. *Phys. Rev. B* **1994**, *49*, 12295.
- (14) Respaud, M.; Broto, J. M.; Rakoto, H.; Fert, A. R.; Thomas, L.; Barbara, B.; Verelst, M.; Snoeck, E.; Lecante, P.; Mosset, A.; Osuna, J.; Ely, T. O.; Amiens, C.; Chaudret, B. *Phys. Rev. B* **1998**, *57*, 2925.
- (15) Deng, J. F.; Yang, J.; Sheng, S. S.; Chen, H. G.; Xiong, G. X. *J. Catal.* **1994**, *150*, 434.

- (16) Deng, J. F.; Li, H. X.; Wang, W. J. *Catal. Today* **1999**, *51*, 113.
- (17) Deng, J. F. *Curr. Top. Catal.* **1999**, *2*, 1.
- (18) Chen, Y. *Catal. Today* **1998**, *44*, 3.
- (19) *Link ISIS Operator's Guide*, revision 3.2; Oxford Instruments PLC: Oxford, U. K., 1997.
- (20) Roucoux, A.; Schulz, J.; Patin, H. *Chem. Rev.* **2002**, *102*, 3757.
- (21) *Handbook of X-ray Photoelectron Spectroscopy*; Perkin-Elmer Corporation: Eden Prairie, MN, 1992.
- (22) Xie, H.; Zhang, B. *J. Mater. Process. Technol.* **2002**, *124*, 8.
- (23) Lee, W. G. In *Proceedings of the 2nd International Congress on Metallic Corrosion*; NACE: Houston, TX, 1963.
- (24) Mallory, G. O.; Hajdu, J. B. *Electroless Plating: Fundamentals and Applications*; American Electroplaters and Surface Finishers Society: Orlando, FL, 1990.
- (25) Shen, J.; Zhang, Q.; Li, Z.; Chen, Y. *J. Mater. Sci. Lett.* **1996**, *15*, 715.
- (26) Hu, Z.; Shen, J. Y.; Chen, Y.; Lu, M.; Hsia, Y. F. *J. Non-Cryst. Solids* **1993**, *159*, 88.
- (27) Hirsh, P.; Howie, A.; Pashley, R. B.; Whelan, M. J.; Kreiger, R. E. *Electron Microscopy of Thin Crystals*; R. E. Krieger Publishing: Huntington, NY, 1977.
- (28) Wonerghem, J.; Mørup, S.; Charles, S. W.; Wells, S. *Nature* **1986**, *322*, 622.
- (29) PDF 4-850 Ni (fcc); PDF 34-501 Ni<sub>3</sub>P (tetragonal); PDF 17-225 Ni<sub>5</sub>P<sub>2</sub> (hexagonal); PDF 22-1190 Ni<sub>12</sub>P<sub>5</sub> (tetragonal).
- (30) Martyak, N. M. *Chem. Mater.* **1994**, *6*, 1667.
- (31) Lambert, M. R.; Duquette, D. J. *Thin Solid Films* **1989**, *177*, 207.
- (32) Tsai, Y. Y.; Wu, F. B.; Chen, Y. I.; Peng, P. J.; Duh, J. G.; Tsai, S. Y. *Surf. Coat. Technol.* **2001**, *146–147*, 502.
- (33) Zhang, B. W.; Hu, W. Y.; Zhang, Q. L.; Qu, X. Y. *Mater. Charact.* **1996**, *37*, 119.
- (34) Hu, C. C.; Bai, A. *Surf. Coat. Technol.* **2001**, *137*, 181.
- (35) Bai, A.; Hu, C. C. *Mater. Chem. Phys.* **2003**, *79*, 49.
- (36) Marshall, G. W.; Lewis, D. B.; Dodds, B. E. *Surf. Coat. Technol.* **1992**, *53*, 223.
- (37) Keong, K. G.; Sha, W.; Malinov, S. J. *Alloys Compd.* **2002**, *334*, 192.
- (38) Hur, S. H.; Jeong, J. H.; Lee, D. N. *J. Mater. Sci.* **1990**, *25*, 2573.
- (39) Ma, E. M.; Luo, S. F.; Li, P. X. *Thin Solid Films* **1988**, *166*, 273.
- (40) Keong, K. G.; Sha, W.; Malinov, S. J. *Mater. Sci.* **2002**, *37*, 4445.
- (41) Gulivets, A. N.; Baskevich, A. S.; Zabludovskii, V. A. *Phys. Met. Metall.* **2004**, *98*, 169.
- (42) Oryshchyn, S.; Babizhetskyy, V.; Chykhriy, S.; Aksel'rud, L.; Stoyko, S.; Bauer, J.; Guérin, R.; Kuz'ma, Y. *Inorg. Mater.* **2004**, *40*, 380.
- (43) Cerezo, A.; Abraham, M.; Clifton, P.; Lane, H.; Larson, D. J.; Petford-Long, A. K.; Thuvander, M.; Warren, P. J.; Smith, G. D. W. *Micron* **2001**, *32*, 731.
- (44) Dean, J. A. *Lange's Handbook of Chemistry*, 15th ed.; McGraw-Hill: New York, 1999.
- (45) Ding, D. Y.; Wang, J. N.; Cao, Z. L.; Dai, J. H.; Yu, F. *Chem. Phys. Lett.* **2003**, *371*, 333.
- (46) Tsai, T. K.; Chuang, C. C.; Chao, C. G.; Liu, W. L. *Diamond Relat. Mater.* **2003**, *12*, 1453.
- (47) De Jong, K. P.; Geus, J. W. *Catal. Rev.* **2000**, *42*, 481.
- (48) Yu, Z.; Chen, D.; Tøtdal, B.; Holmen, A. *J. Phys. Chem. B* **2005**, *109*, 6096.
- (49) Ma, X.; Wang, E. G.; Tilley, R. D.; Jefferson, D. A.; Zhou, W. *Appl. Phys. Lett.* **2000**, *77*, 4136.